

# In Situ Observation of Aggregation of Calcium Aluminate Inclusions at Steel/Ar Interface



JUNTAO BA, QIUYUE ZHOU, YING REN, and LIFENG ZHANG

In the current study, the aggregation of CaO-Al<sub>2</sub>O<sub>3</sub> inclusions with different CaO contents at the steel/Ar interface was *in situ* observed using the confocal laser scanning microscope. The critical acceleration distance and attractive force during the inclusion aggregation process were measured and calculated, and effects of inclusion composition and radius on the aggregation of inclusions were analyzed. When the CaO content in CaO-Al<sub>2</sub>O<sub>3</sub> inclusions in 16Mn steels increased from 3 to 51 pct, inclusions gradually changed from solid to liquid. Solid and partial liquid inclusions aggregated to form large clusters with a maximum diameter of 446.2 μm. When the CaO content in inclusions increased from 3 to 26 pct, the critical acceleration distance between inclusion pairs decreased from 104.9 to 62.1 μm, and the attractive force between inclusion pairs decreased from  $1.0 \times 10^{-16}$  N~ $1.0 \times 10^{-13}$  N to  $1.0 \times 10^{-18}$  N~ $1.0 \times 10^{-15}$  N. As the host inclusion radius increased from 5~15 to 25~35 μm, the critical acceleration distance increased from 104.9 to 166.6 μm. For liquid inclusions, when the CaO content in inclusions increased from 38 to 51 pct, the critical deceleration distance increased from 59.7 to 93.6 μm, and the repulsive force increased from  $1.0 \times 10^{-17}$  N~ $5.0 \times 10^{-15}$  N to  $1.0 \times 10^{-17}$  N~ $1.0 \times 10^{-13}$  N. The liquid inclusion overcame the repulsive force and aggregated, when the host inclusion radius was larger than 10 μm, and the initial velocity of the guest inclusion was faster than 150 μm/s. The calculated attractive force between inclusions was larger than the theoretical value calculated by Kralchevsky-Paunov model.

<https://doi.org/10.1007/s11663-024-03270-4>

© The Minerals, Metals & Materials Society and ASM International 2024

## I. INTRODUCTION

THE calcium treatment of the molten steel was used to improve the castability of the molten steel during the continuous casting process,<sup>[1,2]</sup> prevent the collision and aggregation of inclusions,<sup>[3]</sup> and control the morphology of sulfides in steel.<sup>[4-7]</sup> Inclusions of Al<sub>2</sub>O<sub>3</sub> were modified into CaO·6Al<sub>2</sub>O<sub>3</sub>, CaO·2Al<sub>2</sub>O<sub>3</sub>, and liquid calcium aluminate after the calcium treatment of the Al-killed steel.<sup>[8,9]</sup> Zhang *et al.*<sup>[10,11]</sup> proposed the precise calcium treatment to modify inclusions to the target composition. The contact angle between liquid CaO-Al<sub>2</sub>O<sub>3</sub> inclusions and the molten steel was less than 90 deg, which was difficult to be removed at the

interface of steel and slag.<sup>[12,13]</sup> Large CaO-Al<sub>2</sub>O<sub>3</sub> inclusions were detrimental to properties of pipeline steels and bearing steels.<sup>[14-16]</sup> During the solidification process of the molten steel, the convection of the molten steel and the density difference between inclusions and the molten steel, caused the collision between the inclusions. A part of inclusions were difficult to remove due to the circulating flow, and finally be captured by the solidification front to form inclusion defects.<sup>[17-19]</sup> Especially for heavy ingots, the longer solidification time of the molten steel resulted in stronger collision of inclusions.<sup>[20]</sup>

Yin *et al.*<sup>[21]</sup> firstly observed the aggregation of Al<sub>2</sub>O<sub>3</sub> inclusions at the steel/Ar interface using confocal laser scanning microscopy (CLSM). Inclusions of Al<sub>2</sub>O<sub>3</sub> were easy to aggregated due to the capillary effect, and large clusters with diameter larger than 200 μm were formed within 120s. The attraction between solid inclusions was larger than liquid ones. At the same time, the capillary force also promoted the evolution of inclusion from cluster to single.<sup>[22]</sup> The capillary force was influenced by the size and shape of inclusions<sup>[23]</sup> and the contact angle between inclusions and the molten steel.<sup>[24-26]</sup> Wang *et al.*<sup>[27]</sup> found that the order of the attractive force between the inclusions was Al<sub>2</sub>O<sub>3</sub>>CeAlO<sub>3</sub>, Ce<sub>2</sub>O<sub>3</sub>>Ce<sub>2</sub>O<sub>2</sub>S in Ce-treated steels. Mu *et al.*<sup>[28]</sup> compared the capillary force of different inclusions at the iron/Ar

JUNTAO BA is with the College of Materials Science and Engineering, Yanshan University, Qinhuangdao 066004, P.R. China. QIUYUE ZHOU is with the China Metallurgical Industry Planning and Research Institute, Beijing 100013, P.R. China. YING REN is with the School of Metallurgical and Ecological Engineering, University of Science and Technology Beijing, Beijing 100083, P.R. China. LIFENG ZHANG is with the School of Mechanical and Materials Engineering, North China University of Technology, Beijing 100144, P.R. China. Contact e-mail: zhanglifeng@ncut.edu.cn

Manuscript submitted April 22, 2024; accepted August 25, 2024.

interface, and the order of the capillary force was  $\text{Ce}_2\text{O}_3 > \text{Al}_2\text{O}_3 > \text{Ti}_2\text{O}_3 > \text{MgO} > \text{CaO} > \text{MgAl}_2\text{O}_4 > \text{Al}_2\text{O}_3 > \text{FeO} > \text{MgO} \cdot \text{FeO} > \text{SiO}_2 > \text{TiO}_2$ . Wang *et al.*<sup>[29]</sup> found that the larger radius of solid inclusions, the greater contact angle between inclusions and the molten steel, promoting the greater collision of inclusions. Duan *et al.*<sup>[30]</sup> found that the critical aggregation distance between solid inclusions was proportional to the radius of inclusions. In addition, the Kralchevsky-Paunov model was widely used to explain the capillary force between inclusions, while the attractive force calculated by the Kralchevski-Paunov model was smaller than the actual value.<sup>[31]</sup> Qiu *et al.*<sup>[32,33]</sup> developed a sub-particle model based on the Kralchevsky-Paunov model. The large inclusion was considered to be a cluster of small sub-particles. At present, many *in situ* observations experiments were carried out to observe the collision of solid inclusions, while the aggregation between semi-solid and liquid inclusions was rarely studied.<sup>[34]</sup>

Three types of inclusions were detected in the molten steel after the calcium treatment, including solid, partial-liquid and liquid inclusion.<sup>[35]</sup> In the current study, in order to study the effect of CaO content in calcium aluminate inclusions on the aggregation of inclusions, the aggregation process of different types of CaO-Al<sub>2</sub>O<sub>3</sub> inclusions at the liquid steel/Ar interface was *in situ* observed using confocal laser scanning microscopy. The critical acceleration distance and attractive force of aggregation process of inclusions were measured and calculated. Moreover, the effect of inclusion composition and radius on the attractive force of inclusions was analyzed.

## II. METHODOLOGY

The production route of the 16Mn steel was produced by the EAF-LF-VD-Ingot casting. The calcium treatment was conducted after the vacuum treatment in VD. Steel samples were taken before and after the calcium treatment, which was mentioned in the previous study.<sup>[6]</sup> The composition and diameter of inclusions in the steel were detected by scanning electron microscope(SEM). The composition and parameters of CaO-Al<sub>2</sub>O<sub>3</sub> inclusions before the aggregation are summarized in Table I. The average diameter of CaO-Al<sub>2</sub>O<sub>3</sub> inclusions before the aggregation was 3.1~3.7  $\mu\text{m}$ , and the maximum diameter of inclusions increased with the increase of CaO content in inclusions. The inclusions in the region upon the liquidus were fully liquid inclusions, while 100 pct alumina inclusions were pure solid inclusions. Therefore, inclusions between those two states were defined as partial-liquid inclusions in this study. With the increase of CaO content in inclusions from 3.6 to 51.3 pct, the contact angle between inclusions and the molten steel decreased from 124.9 to 61.4 deg, the CaO-Al<sub>2</sub>O<sub>3</sub> inclusions gradually changed from solid to liquid. The contact angle of inclusions with different contents was calculated using Eq. [1].<sup>[36]</sup>

$$\alpha = 47.689 \left( \frac{w_{\text{CaO}}}{w_{\text{Al}_2\text{O}_3}} \right)^2 - 113.26 \frac{w_{\text{CaO}}}{w_{\text{Al}_2\text{O}_3}} + 128.58 \quad [1]$$

where  $\alpha$  is the contact angle in deg and  $w$  is the mass fraction.

The schematic of the inclusion aggregation mechanism during CLSM experiment is shown in Figure 1. A cylindrical sample with a diameter of 8 mm was taken from the steel bucket sample along the axial direction, and then a number of small samples with a size of  $\varnothing 8 \text{ mm} \times 4 \text{ mm}$  were divided. Small steel samples were polished and placed in an Al<sub>2</sub>O<sub>3</sub> crucible. The density of inclusions was smaller than that of the molten steel. After the melting of steel, inclusions floated to the steel/Ar interface.

The temperature curve of the current inclusion aggregation experiment is shown in Figure 2. The steel sample was heated to 1673 K at the rate of 300 K/min. In order to prevent the sample from completely melting due to the fast heating rate, the sample was then heated to 1823 K at the rate of 100 K/min. Each steel sample was observed for 20~30 min and the image of inclusion aggregation was recorded every 0.02s. After the observation, the sample was cooled at the rate of 500 K/min. The morphology of inclusions after the aggregation in the solidified sample were observed using SEM.

## III. COMPOSITION AND MORPHOLOGY OF INCLUSIONS BEFORE AGGREGATION

The composition distribution of inclusions before aggregation is shown in Figure 3. The original composition of inclusions in sample 1 is shown in Figure 3(a). The average composition of inclusions was 3.6 pct CaO-85.9 pct Al<sub>2</sub>O<sub>3</sub>-7.1 pct MgO-3.4 pct SiO<sub>2</sub>, and inclusions were solid in the molten steel. The CaO content of inclusions in samples was 16.5 and 26.1 pct inclusions were partial liquid. Average compositions of inclusions in sample 4 and 5 were 37.8 pct CaO-47.1 pct Al<sub>2</sub>O<sub>3</sub>-8.6 pct MgO-6.5 pct SiO<sub>2</sub> and 51.3 pct CaO-30.5 pct Al<sub>2</sub>O<sub>3</sub>-7.8 pct MgO-10.4 pct SiO<sub>2</sub>, respectively. Inclusions in sample 4 and 5 were pure liquid.

The morphology of CaO-Al<sub>2</sub>O<sub>3</sub> inclusions with different CaO contents before aggregation is shown in Figure 4. Solid inclusions were black and in irregular, which were composed of the MgO-Al<sub>2</sub>O<sub>3</sub> spinel core and the CaO-Al<sub>2</sub>O<sub>3</sub> outer layer. Inclusions containing 16 pct CaO were mainly irregular. As the CaO content in inclusions increased to 26 pct, inclusions became dark gray and spherical. Spherical inclusions containing 38 pct CaO and 51 pct CaO were liquid with homogeneous calcium aluminate inclusions.

The aggregation of CaO-Al<sub>2</sub>O<sub>3</sub> inclusions with different CaO contents observed using CLSM is shown in Figure 5. The shooting frequency was 5 pictures per second. Thus, there was ghost in the shot picture due to the faster movement speed of the inclusion and high shooting frequency. In the distance measurement based on the picture, samples of inclusions with the maximum moving speed are taken consistently before and after. The aggregation process of solid inclusions containing 3 pct CaO is shown in Figure 5(a). Two small clusters with the radius of 20.9 and 15.6  $\mu\text{m}$ , began to accelerate

**Table I. The Composition and Parameters of CaO-Al<sub>2</sub>O<sub>3</sub> Inclusions Before Aggregation**

Sample	Average Composition (pct)				Number Density (#/mm <sup>2</sup> )	Diameter (μm)	Contact Angle (°)	State
	CaO	Al <sub>2</sub> O <sub>3</sub>	MgO	SiO <sub>2</sub>				
1	3.6	85.9	7.1	3.4	10.4	3.1	124.9	solid
2	16.5	77.4	5.0	1.1	16.0	3.1	107.6	partial-liquid
3	26.1	55.8	10.8	7.3	7.4	3.7	92.7	partial-liquid
4	37.8	47.1	8.6	6.5	9.5	3.3	74.3	liquid
5	51.3	30.5	7.8	10.4	8.43	3.3	61.4	solid

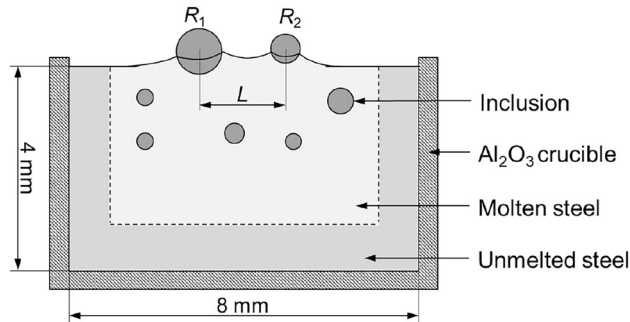


Fig. 1—Schematic of the CSLM experiment.

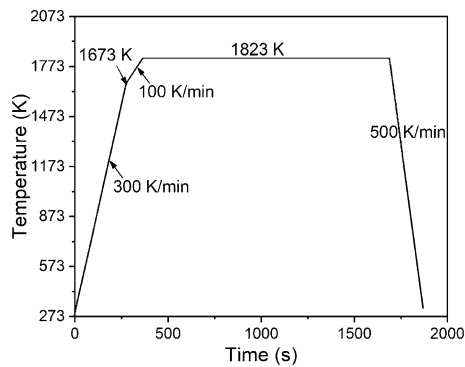


Fig. 2—The temperature curve of the inclusion aggregation experiment.

at a distance of 113.1 μm, then aggregated into a large cluster after 1.24s. The aggregation process of partial-liquid inclusions containing 26 pct CaO is shown in Figure 5(c). Two inclusions with equivalent radius of 7.0 and 4.7 μm began to accelerate at a distance of 66.7 μm and aggregated into a large inclusion after 1.10 s. The aggregation process of liquid inclusions containing 38 pct CaO is shown in Figure 5(d). Two inclusions with the equivalent radius of 8.5 and 10.4 μm aggregated within 0.2 s, forming a inclusion with the equivalent radius of 11.2 μm. Subsequently, the formed inclusion aggregated with another inclusion within 0.42s. The

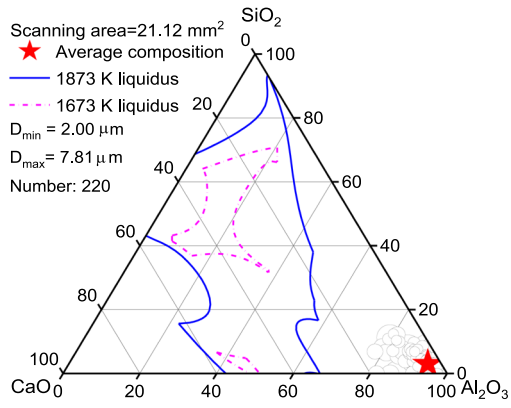
aggregation process of liquid inclusions containing 51 pct CaO was similar to that of inclusions containing 38 pct CaO. When the radius of the main inclusion in the liquid inclusion was larger than 10 μm and the speed of the guest inclusion was greater than 150 μm/s, the inclusion can overcome the repulsive force and aggregated. The diameter of formed inclusions slightly increased after the aggregation of liquid inclusions.

*In situ* observation of the repulsion process of liquid CaO-Al<sub>2</sub>O<sub>3</sub> inclusions is shown in Figure 6. When the large spherical inclusions collided with each other, the aggregation of inclusion can hardly be observed, and then inclusions were repulsed and gradually moved away from each other. The aggregation or repulsion between liquid inclusions was directly related to the state of inclusions before collision. When inclusions moved gently, liquid calcium aluminate inclusions can hardly aggregate together.

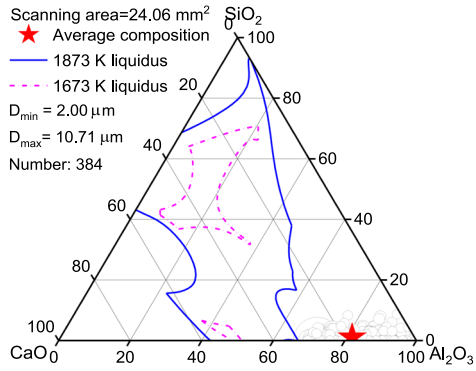
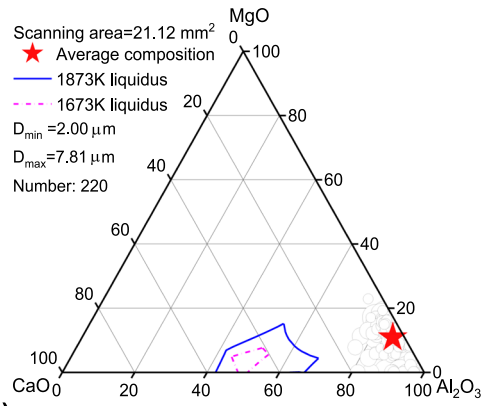
The variation of the average radius of different CaO-Al<sub>2</sub>O<sub>3</sub> inclusions during the aggregation process is shown in Figure 7. Through 10 min collision and aggregation, the radius of solid inclusions containing 3 pct CaO increased from 8.9 to 24.0 μm, while the radius of solid inclusions containing 51 pct CaO increased from 6.5 to 10.4 μm. Due to the difference of initial diameter in 16 pct CaO and 26 pct CaO, the inclusion size formed after collisions was larger in 26 pct CaO. Moreover, the inevitable error in the experimental process may also lead to the above phenomenon. Therefore, with the increase of CaO content in inclusions, the increase of the inclusion radius in the aggregation process became smaller.

The morphology of different CaO-Al<sub>2</sub>O<sub>3</sub> inclusions in solidified samples is shown in Figure 8. Large clusters were formed after the aggregation of solid inclusions. Partial liquid inclusions containing 16 pct CaO formed small clusters. Inclusions containing 26 pct CaO were irregular. The liquid inclusions containing 38 pct and 51 pct CaO were spherical.

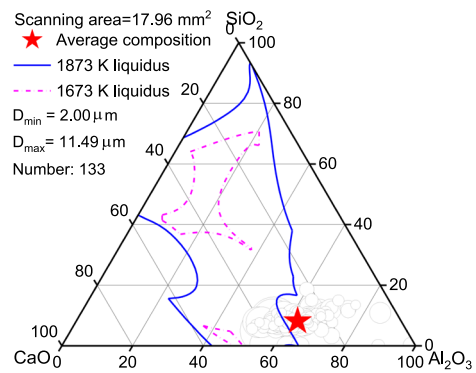
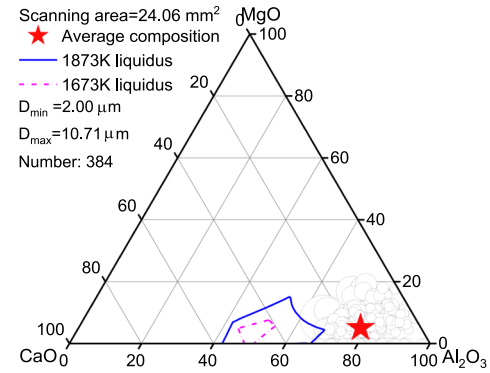
The effect of CaO content on the maximum diameter of inclusions after the aggregation is shown in Figure 9. With the increase of CaO content in inclusions from 3 to 51 pct, the maximum diameter of inclusions formed after the collision decreased from 446.2 to 46.3 μm. When the CaO content in inclusions increased to larger than 26 pct, the maximum diameter of inclusions formed after the collision decreased.



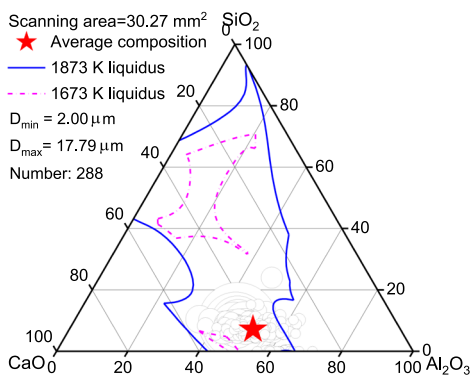
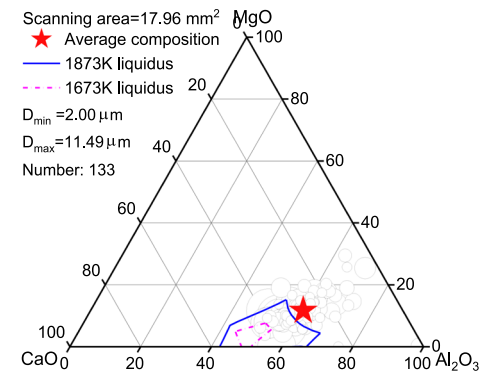
(a)



(b)



(c)



(d)

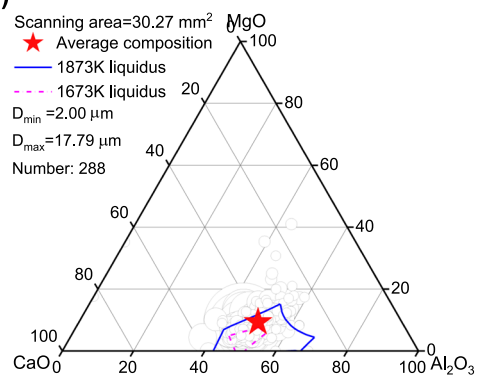


Fig. 3—The average composition of inclusions with various CaO contents before collision, (a) 3 pct, (b) 16 pct, (c) 26 pct, (d) 38 pct, and (e) 51 pct.

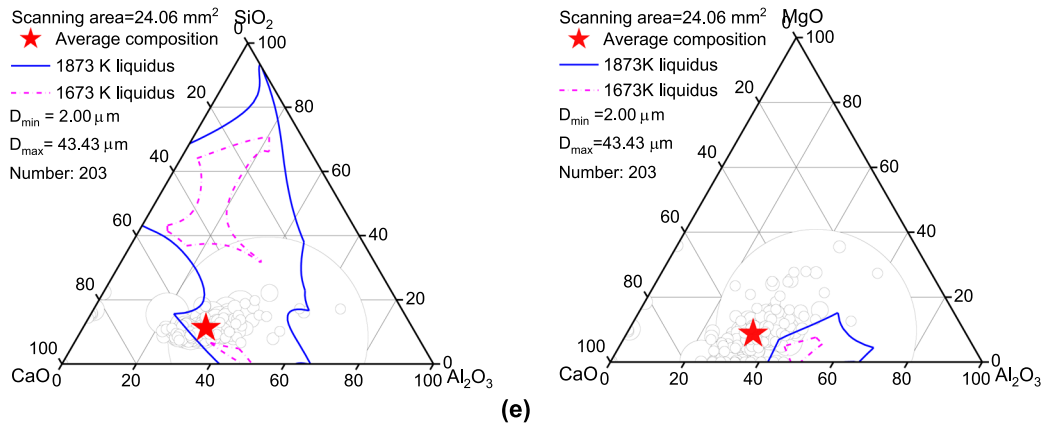


Fig. 3—continued.

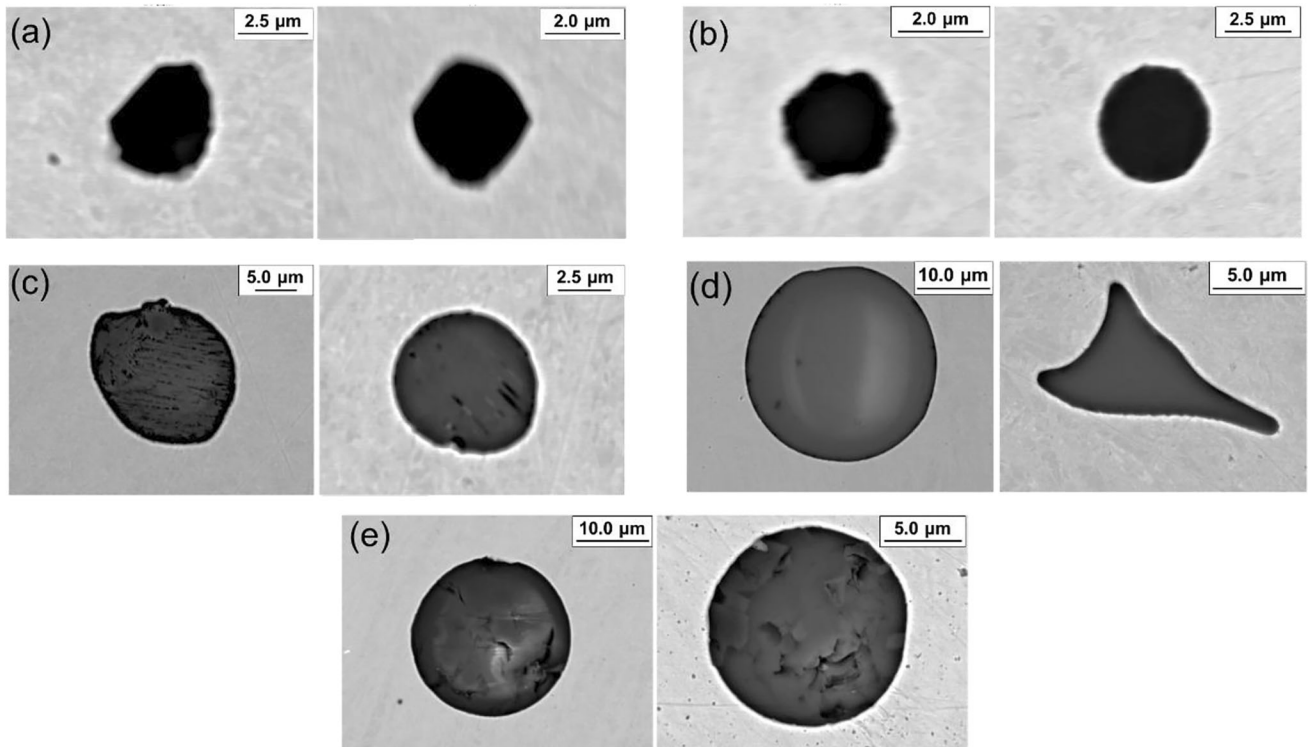


Fig. 4—The morphology of different CaO-Al<sub>2</sub>O<sub>3</sub> inclusions with various CaO contents before collision (a) 3 pct, (b) 16 pct, (c) 26 pct, (d) 38 pct, and (e) 51 pct.

#### IV. ATTRACTIVE FORCE BETWEEN INCLUSIONS

Schematic of the distance between inclusions during the collision process is shown in Figure 10. The larger and stationary inclusion was defined as the host inclusion with a radius of  $R_1$ , and the smaller and moving inclusion was defined as the guest inclusion with a radius of  $R_2$ . When the guest inclusion moved to the main inclusion, the attractive force between inclusions was calculated by Newton's second law.

The irregular inclusion was assumed to be spherical, and the equivalent diameter of the inclusion is calculated by Eq. [2]. Velocities of the guest inclusions at time 1 and time 2 are calculated by Eqs. [3] through [4]. The acceleration of the guest inclusion during the movement is calculated by Eq. [5]. The mass of the guest inclusions is calculated by Eq. [6]. The attractive force is calculated using Newton's second law by Eq. [7]. When two inclusions moved close to each other, a modified calculation formula is used, as shown in Eq. [8].

$$R_2 = \sqrt{\frac{Area}{4\pi}} \quad [2]$$

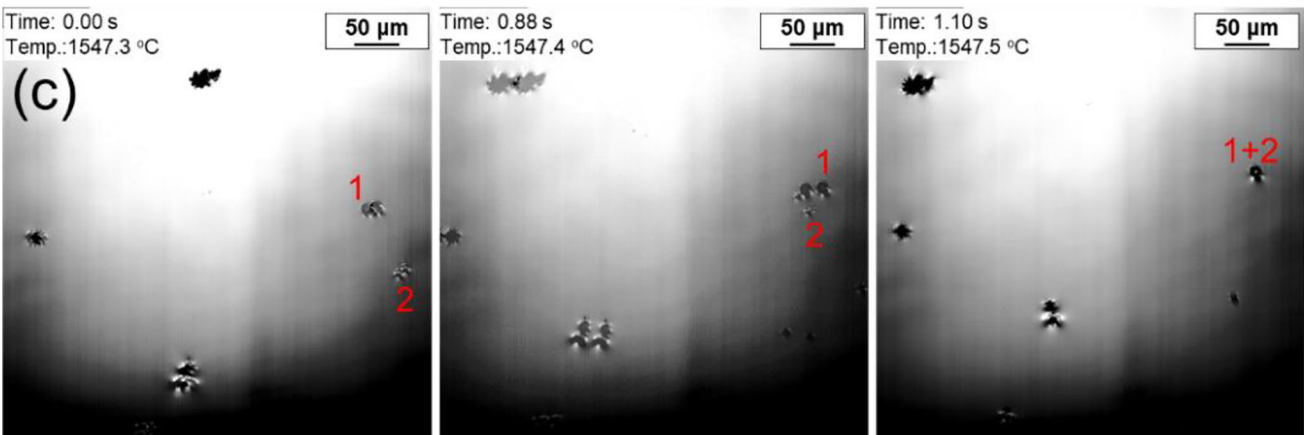
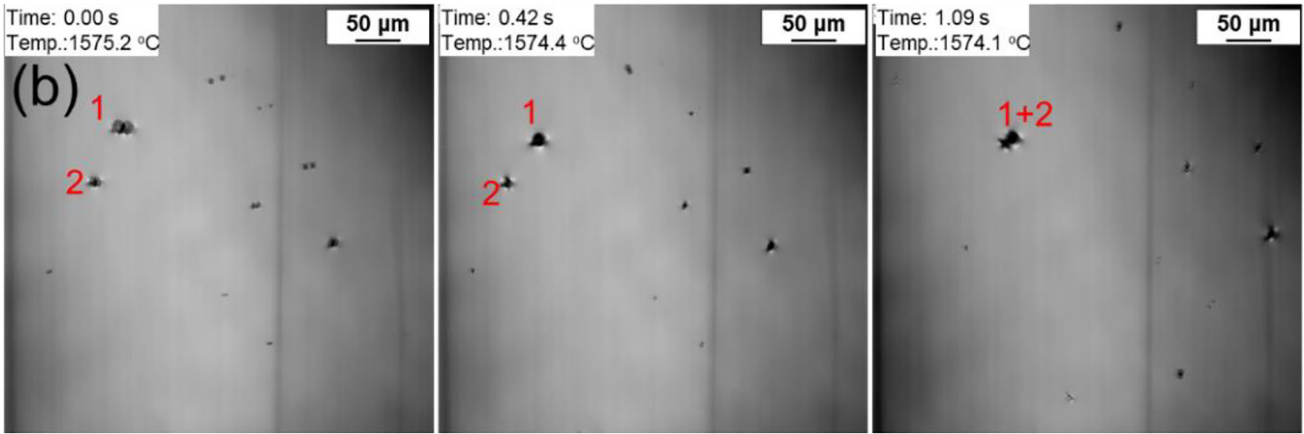
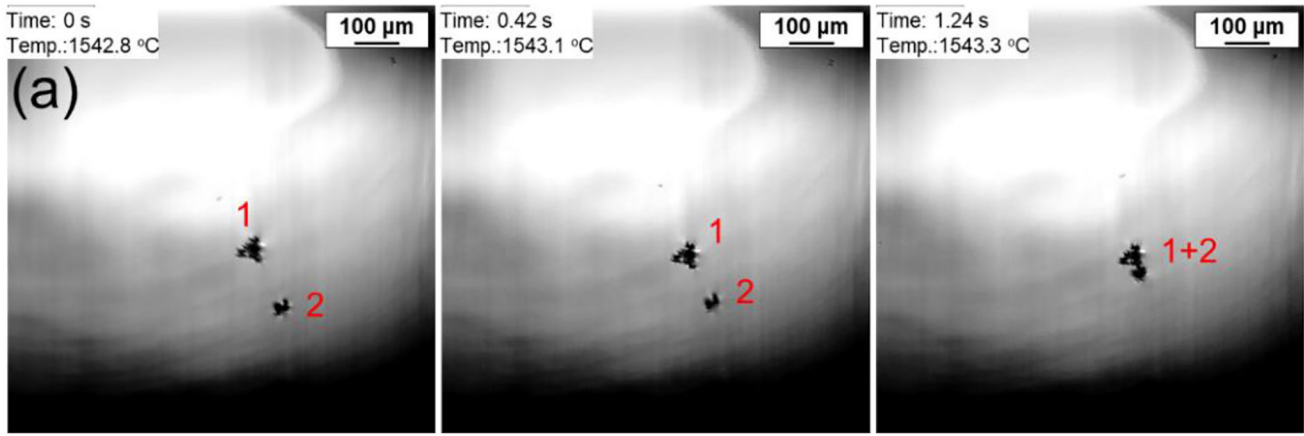


Fig. 5—*In situ* observation of the aggregation of CaO-Al<sub>2</sub>O<sub>3</sub> inclusions with different CaO contents, (a) 3 pct, (b) 16 pct, (c) 26 pct, (d) 38 pct, and (e) 51 pct.

$$v_1 = \frac{L_1 - L_2}{\Delta t} \quad [3]$$

$$a_2 = \frac{v_2 - v_1}{\Delta t} \quad [5]$$

$$v_2 = \frac{L_2 - L_3}{\Delta t} \quad [4]$$

$$m_2 = \frac{4}{3} \pi R_2^3 \cdot \rho_{inc} \quad [6]$$

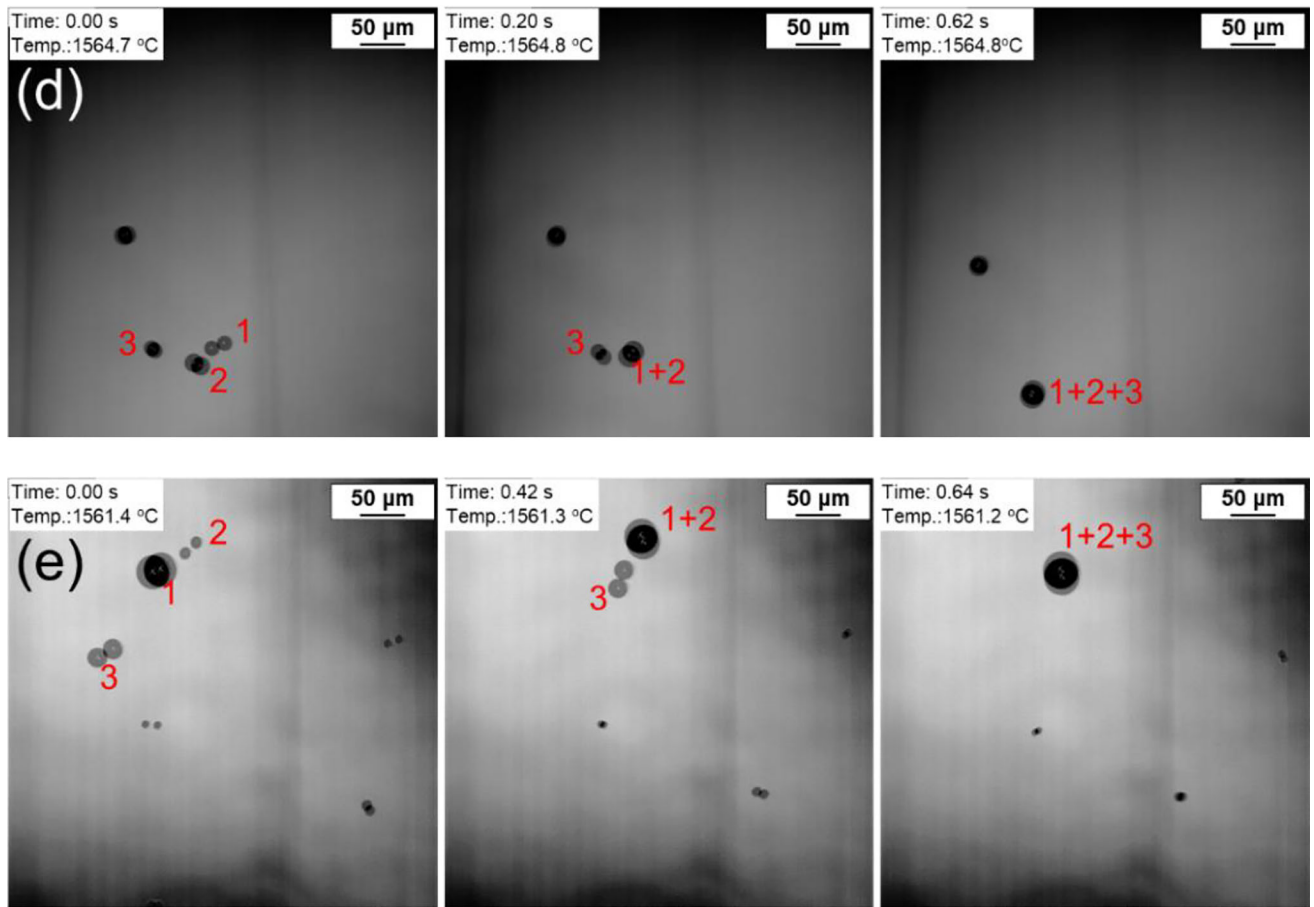


Fig. 5—continued.

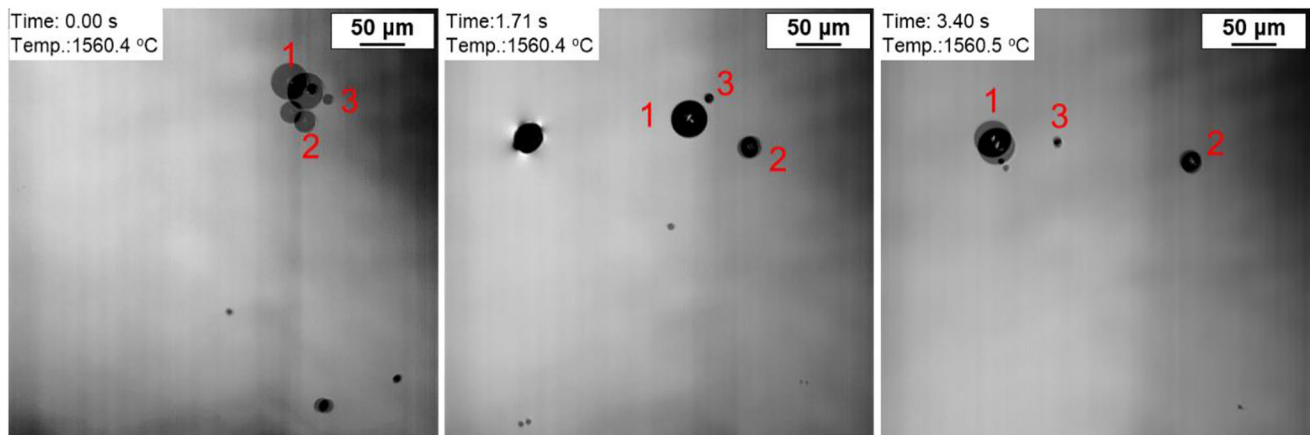


Fig. 6—*In situ* observation of the repulsion process of liquid CaO-Al<sub>2</sub>O<sub>3</sub> inclusions.

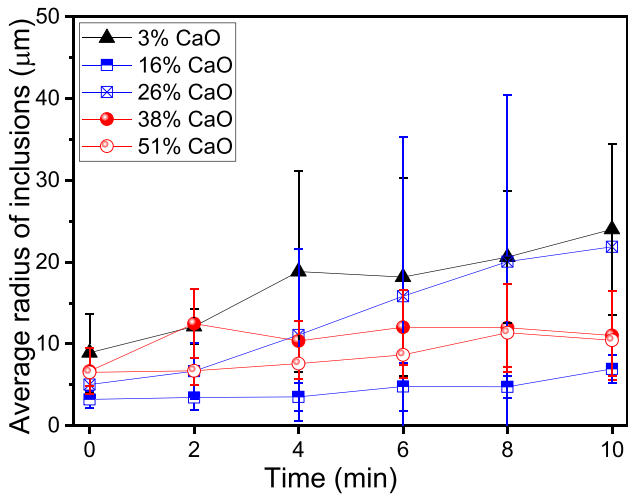


Fig. 7—The variation of the average radius of different CaO-Al<sub>2</sub>O<sub>3</sub> inclusions during the aggregation process.

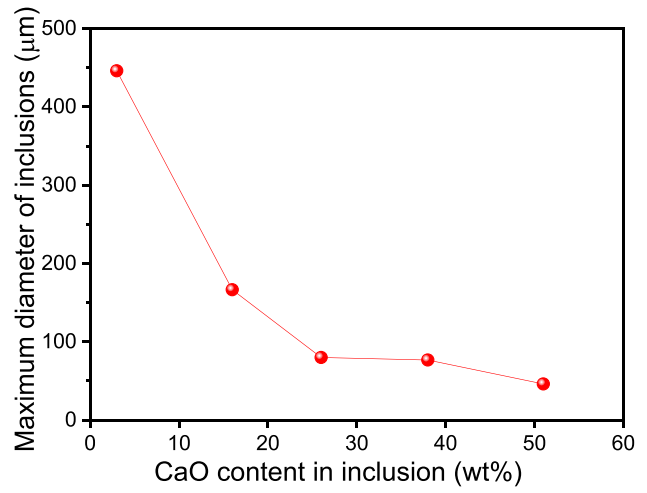


Fig. 9—The effect of CaO content on the maximum diameter of inclusions after the aggregation.

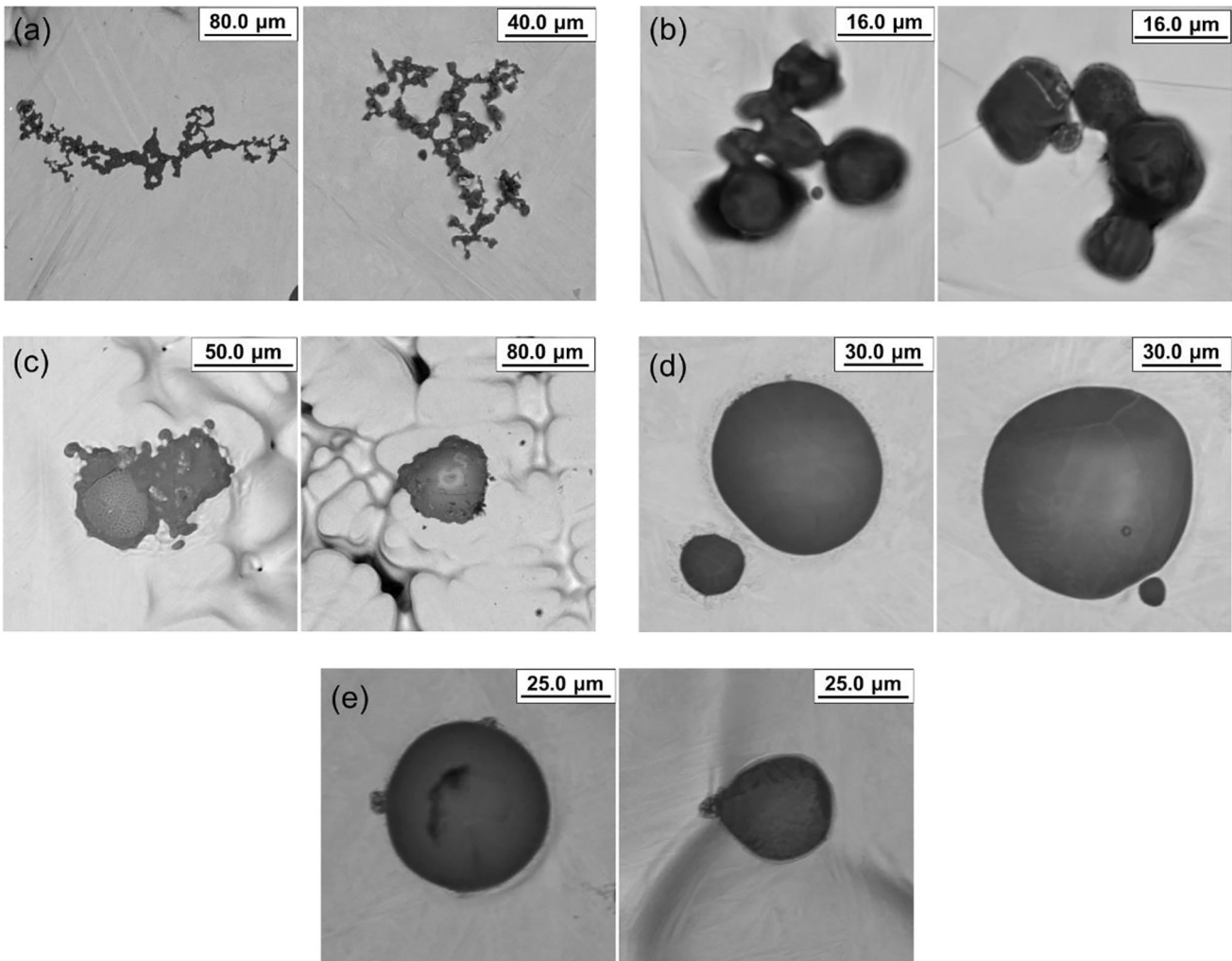


Fig. 8—The morphology of different CaO-Al<sub>2</sub>O<sub>3</sub> inclusions with various CaO contents, (a) 3 pct, (b) 16 pct, (c) 26 pct, (d) 38 pct, and (e) 51 pct.



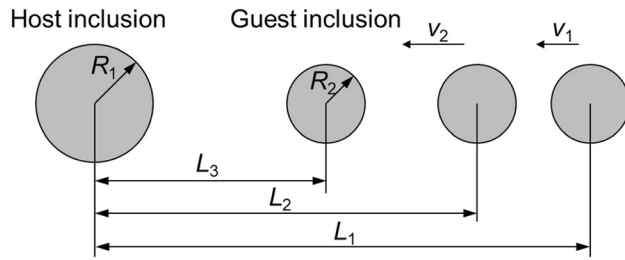


Fig. 10—The schematic of the variation of the distance between inclusions during the collision process.

$$F = m_2 \times a_2 \quad [7]$$

$$F = a_2 \times \frac{m_1 \times m_2}{m_1 + m_2} \quad [8]$$

where  $R_2$  is the diameter of the guest inclusion, m;  $Area$  is the area of the guest inclusion,  $m^2$ ;  $L_1$  is the distance between the inclusion pairs at time 1, m;  $L_2$  is the distance between the inclusion pairs at time 2, m;  $L_3$  is the distance between the inclusions in time 3, m;  $v_1$  is the average velocity of inclusions between time 1 and time 2, m/s;  $v_2$  is the average velocity of inclusions between time 2 and time 3, m/s;  $a_2$  is the acceleration of inclusions from time 1 to time 3,  $m/s^2$ ;  $m_1$  is the mass of the host inclusion, kg;  $m_2$  is the mass of inclusions, kg;  $F$  is the attractive force between two inclusions, N;  $\rho_{inc}$  is the density of inclusions,  $kg/m^3$ .

ImageJ software was used to measure the equivalent radius of inclusions and the distance between inclusions at different times observed using CLSM, as shown in Figure 11. Solid inclusions containing 3 pct CaO began to accelerate when the distance was less than  $150 \mu m$ , and inclusions collided and aggregated within 1.4s. Partial liquid inclusions containing 16 pct CaO and 26 pct CaO began to accelerate when the distance was less than  $120 \mu m$ , and aggregated within 1.7s. The variation of the distance between liquid calcium aluminate inclusions with time during the collision process is shown in Figures 11(d) through (e). The collision and aggregation occurred when the radius of the host inclusion was larger than  $10 \mu m$  and the initial velocity of the host inclusion was faster than  $150 \mu m/s$ . Due to the repulsion between liquid inclusions, the speed of inclusions decreased with the decrease of the distance. In addition, the smaller size of the guest inclusion, the longer time required for the collision and aggregation. With the increase of CaO content in inclusions, the motion state between inclusion pairs changed from acceleration to deceleration, inclusion pairs changed from attraction to mutual exclusion.

The acceleration of CaO- $Al_2O_3$  inclusions varied with the distance in the aggregation process is shown in Figure 12. The acceleration increased gradually with the decrease of the distance between inclusion pairs for solid inclusions and half liquid inclusions. When the CaO content in inclusions increased from 3 to 26 pct, the

average acceleration decreased from  $3.9 \times 10^{-5} m/s^2$  to  $1.7 \times 10^{-5} m/s^2$  with the distance between two inclusions of  $50 \mu m$ . For liquid inclusions, the acceleration gradually decreased with the decrease of distance. The acceleration of most inclusions was negative when the distance between inclusions was less than  $50 \mu m$ , indicating inclusions were decelerated by repulsion. For liquid inclusions containing 51 pctCaO, the acceleration decreased with the smaller distance of less than  $80 \mu m$ . For liquid inclusions, collision and aggregation occurred when the initial velocity of inclusions was large.

The comparison of attractive and repulsive force between different CaO- $Al_2O_3$  inclusions is shown in Figure 13. The attractive force between solid inclusions containing 3 pct CaO was  $1.0 \times 10^{-16} N \sim 1.0 \times 10^{-13} N$ . The attractive force between the half liquid inclusions containing 16 pct CaO and 26 pct CaO was  $1.0 \times 10^{-18} N \sim 1.0 \times 10^{-15} N$ . The repulsive force between liquid inclusions also increased with the decrease of distance. The repulsive force between liquid inclusions containing 38 pct CaO was  $1.0 \times 10^{-17} N \sim 5.0 \times 10^{-15} N$ , and it was  $1.0 \times 10^{-17} N \sim 1.0 \times 10^{-13} N$  for liquid inclusions containing 51 pct CaO. With the increase of CaO content in inclusions, the attractive force decreased, and when inclusions change into liquid calcium aluminate, inclusions began to repel each other after inclusions were modified to liquid.

The effect of the host inclusion radius on the attractive force is shown in Figure 14. As the radius of the host inclusion increased from  $5 \sim 15$  to  $25 \sim 35 \mu m$ , the attractive force between inclusions increased from  $1.0 \times 10^{-16} N \sim 1.0 \times 10^{-14} N$  to  $1.0 \times 10^{-15} N \sim 1.0 \times 10^{-13} N$ . Therefore, for solid inclusions, the larger size, the larger attractive force between two inclusions.

The effect of the host inclusion radius on the average critical acceleration distance is shown in Figure 15. The critical acceleration distance of the aggregation of inclusions was mainly related to the host inclusion size, which was hardly influenced by the guest inclusion size. As the radius of the host inclusion increased from  $5 \sim 15$  to  $25 \sim 35 \mu m$ , the critical acceleration distance increased from  $104.9$  to  $166.6 \mu m$ . The larger size of inclusions, and the faster size growth rate.

The effect of CaO content in inclusions on the critical acceleration distance is shown in Figure 16. When the CaO content in solid and half liquid inclusions increased from 3 to 26 pct, the contact angle between inclusions and the molten steel decreased from  $124.9$  to  $92.7$  deg, and the critical acceleration distance decreased from  $104.9$  to  $62.1 \mu m$ . When the CaO content in liquid inclusions increased from 38 to 51 pct, the contact angle between inclusions and the molten steel decreased from  $74.3$  to  $61.4$  deg, and the critical deceleration distance increased from  $59.7$  to  $93.6 \mu m$ .

The Kralchevsky-Paunov model<sup>[37]</sup> was used to calculate the theoretical capillary attractive force between two floating inclusions by Eqs. [9] through [12]. The effect of CaO content of inclusions on the attractive force is show in Figure 17. The attractive force between inclusions calculated in the experiment

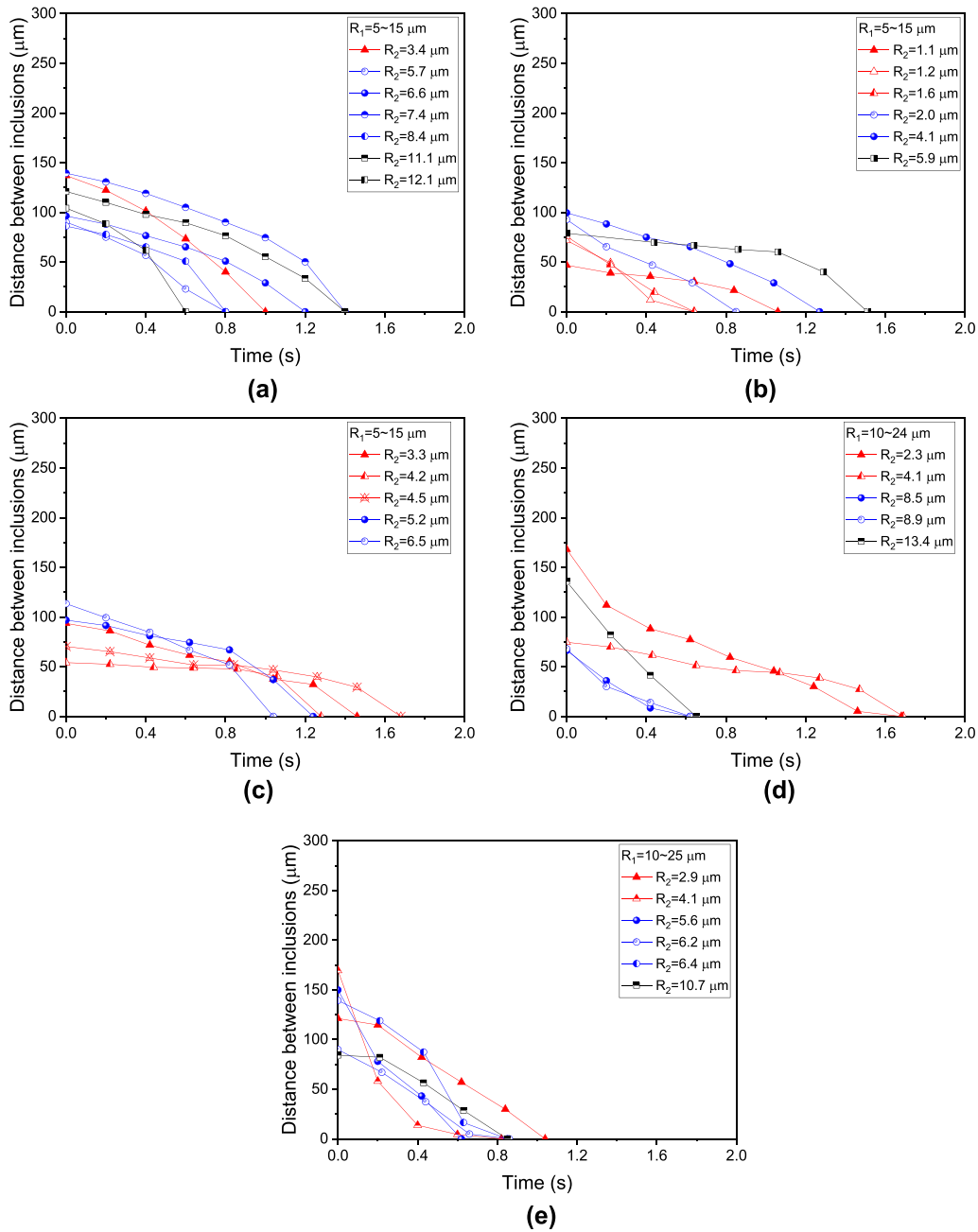


Fig. 11—Variation of the distance between inclusions with various CaO contents with time during the collision process, (a) 3 pct, (b) 16 pct, (c) 26 pct, (d) 38 pct, and (e) 51 pct.

was larger than the theoretical value, because the inclusion changed the movement direction in the aggregation process and the inclusion was also attracted by other inclusions in steel.<sup>[38]</sup> For the radius of both the host inclusion and the guest inclusion was  $10 \mu\text{m}$  and the distance of  $50 \mu\text{m}$ , the theoretical attraction between inclusions decreased from  $1.3 \times 10^{-15} \text{ N}$  to  $2.3 \times 10^{-17} \text{ N}$  when the CaO content

increased from 3 to 26 pct. When the CaO content in liquid inclusions increased from 38 to 51 pct, the theoretical repulsive force between inclusions increased from  $2.2 \times 10^{-16} \text{ N}$  to  $7.5 \times 10^{-16} \text{ N}$ . The CaO content in liquid inclusions had little effect on the repulsive force between inclusions. The repulsive force between inclusions was in the same order of magnitude, which was consistent with experimental results.

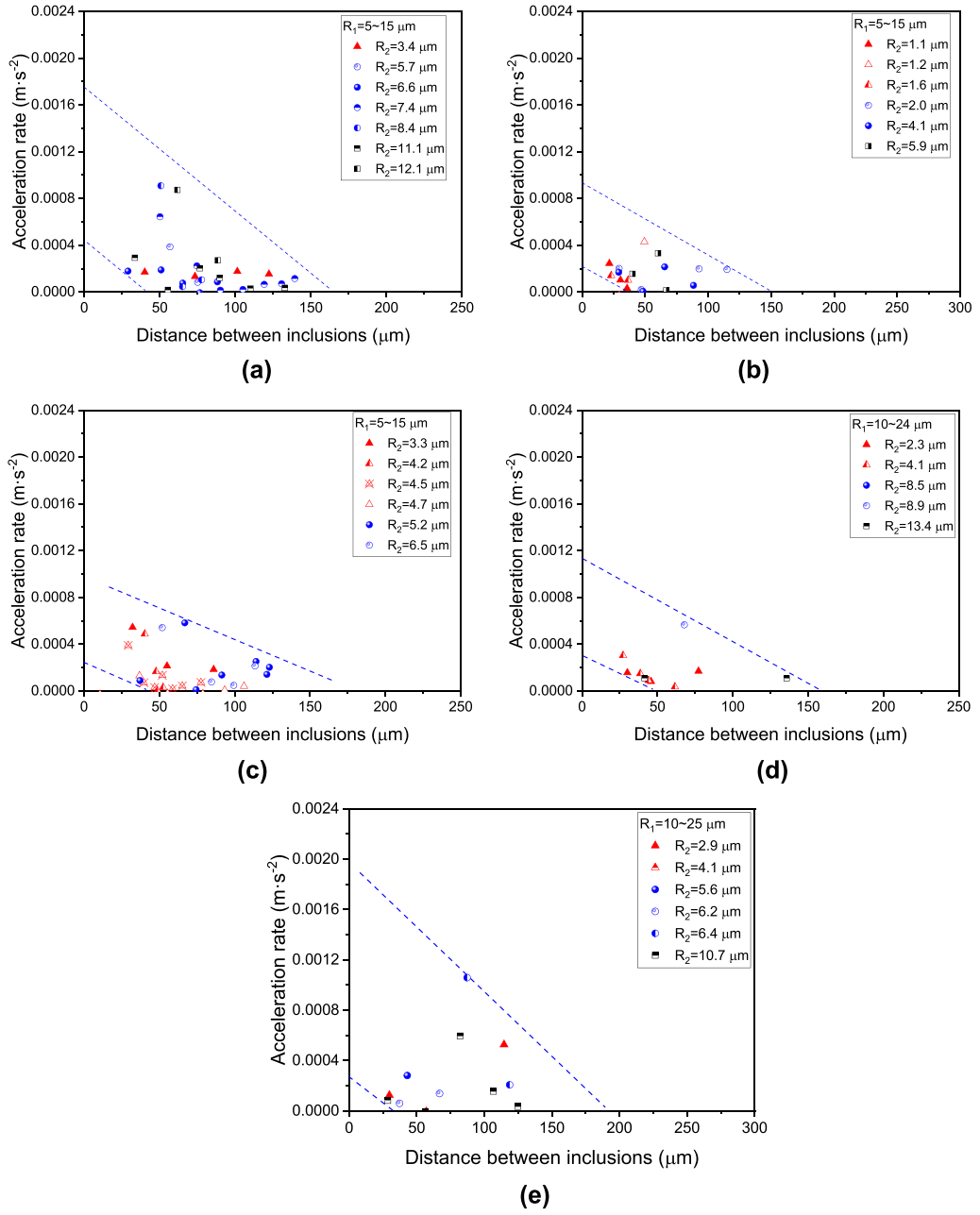


Fig. 12—The acceleration rate of different CaO-Al<sub>2</sub>O<sub>3</sub> inclusions with different contents varied with distance in aggregation process, (a) 3 pct, (b) 16 pct, (c) 26 pct, (d) 38 pct, and (e) 51 pct.

$$F = 2\pi\gamma \frac{Q_1 Q_2}{L}, 2r_c < L < q^{-1} \quad [9]$$

$$Q_1 = \frac{1}{3} \pi q^2 R_1^3 (2 - 4S_{\text{inc}} + \cos \theta - \cos^3 \theta) \quad [10]$$

$$q = \sqrt{\frac{(\rho_{\text{steel}} - \rho_{\text{Ar}})g}{\gamma}} \quad [11]$$

$$S_{\text{inc}} = \frac{\rho_{\text{inc}} - \rho_{\text{Ar}}}{\rho_{\text{steel}} - \rho_{\text{Ar}}} \quad [12]$$

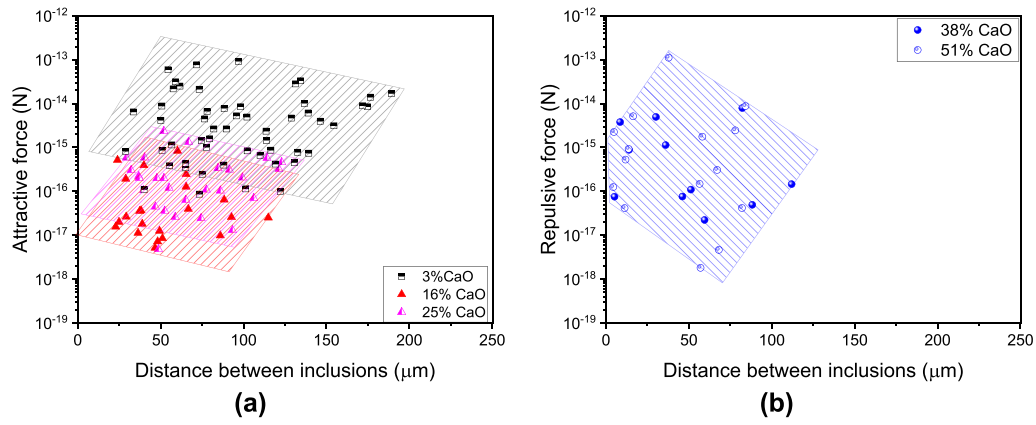


Fig. 13—The comparison of forces between different CaO-Al<sub>2</sub>O<sub>3</sub> inclusions, (a) the attractive force, (b) the repulsive force.

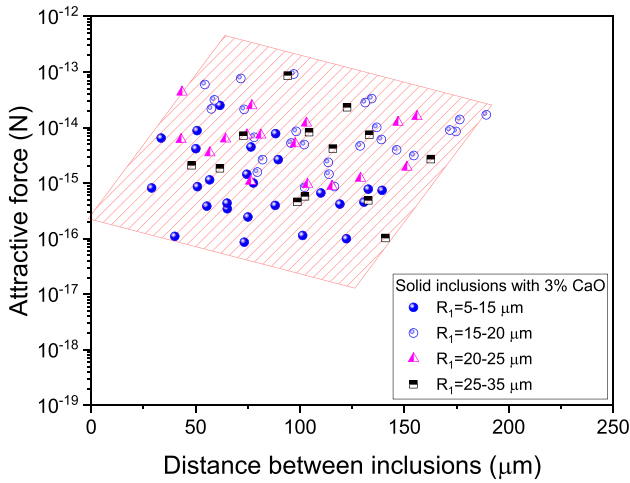


Fig. 14—The effect of the host inclusion radius on the attractive force between inclusion pairs.

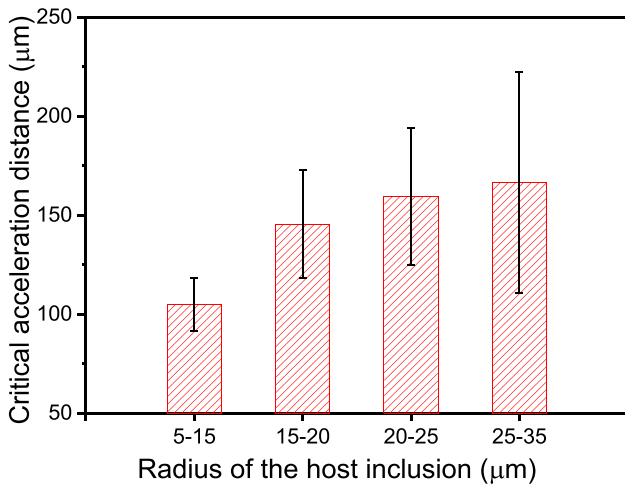


Fig. 15—The effect of the host inclusion radius on the average critical acceleration distance.

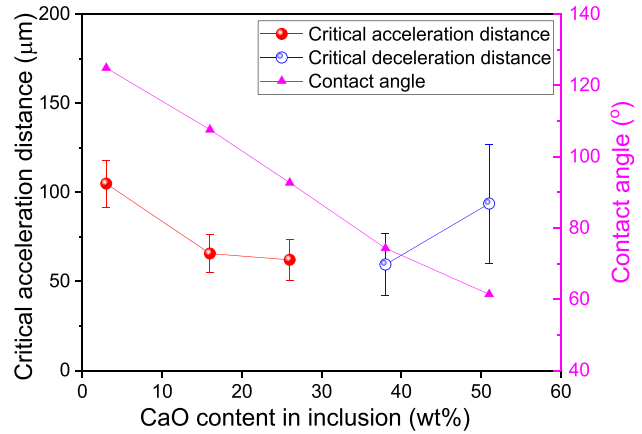


Fig. 16—The effect of CaO content in inclusions on the critical acceleration or deceleration distance.

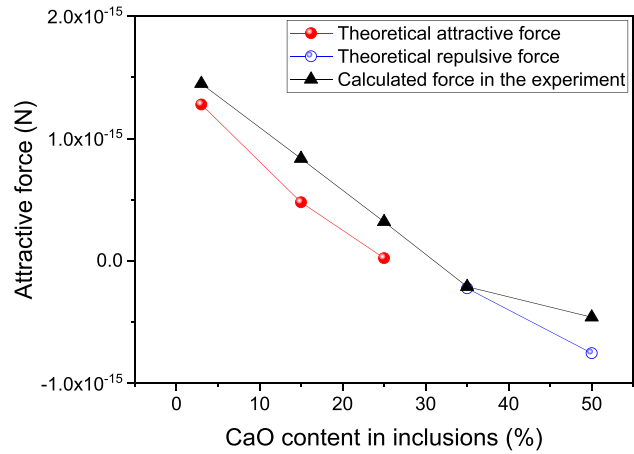


Fig. 17—The effect of the CaO content of inclusions on the attractive force.

where  $\gamma$  is the interfacial tension, N/m;  $L$  is the distance between floating inclusion 1 and inclusion 2, m;  $Q_1$  is the ‘capillary charge’ of inclusion 1, m;  $q$  is the capillary action distance,  $m^{-1}$ ;  $R_1$  is the radius of inclusion 1, m;  $\theta$  is the three-phase contact angle, deg;  $\rho_{\text{steel}}$  is the density of the molten steel,  $kg/m^3$ ;  $\rho_{\text{Ar}}$  is the density of argon,  $kg/m^3$ ;  $S_{\text{inc}}$  is the ratio of the density difference between the inclusion and argon to the density difference between the liquid steel and argon.

## V. CONCLUSIONS

The aggregation of calcium aluminum inclusions were *in situ* observed to study the effect of the CaO content on the aggregation of inclusions at the steel/Ar interface. Following conclusions were obtained.

- (1) Solid inclusions were easy to aggregate, and large clusters with a maximum diameter of  $446.2 \mu\text{m}$  can be formed after the aggregation for 21 min. Half liquid inclusions containing 16 pct CaO and 26 pct CaO also aggregated, leading to the formation of small cluster or irregular inclusion. Liquid inclusions containing 38 pct CaO and 51 pct CaO repelled each other. When the radius of the host inclusion was larger than  $10 \mu\text{m}$ , and the initial velocity of the guest inclusion was faster than  $150 \mu\text{m/s}$ , the inclusion overcame the repulsive force and aggregated.
- (2) For solid and half liquid inclusions, the increase of radius of the inclusion in the aggregation process decreased with the increase of CaO content. When the CaO content in inclusions increased from 3 to 26 pct, the critical acceleration distance of the aggregation decreased from  $104.9$  to  $62.1 \mu\text{m}$ , and the attraction range between inclusion pairs decreased from  $1.0 \times 10^{-16} \text{ N}$ – $1.0 \times 10^{-13} \text{ N}$  to  $1.0 \times 10^{-18} \text{ N}$ – $1.0 \times 10^{-15} \text{ N}$ . With the increase of the radius of the host inclusion, the critical acceleration distance increased.
- (3) For liquid inclusions, when the CaO content in inclusions increased from 38 to 51 pct, the critical deceleration distance increased from  $59.7$  to  $93.6 \mu\text{m}$ , and the range of the repulsive force between inclusions increased from  $1.0 \times 10^{-17} \text{ N}$ – $5.0 \times 10^{-15} \text{ N}$  to  $1.0 \times 10^{-17} \text{ N}$ – $1.0 \times 10^{-13} \text{ N}$ .

## ACKNOWLEDGMENTS

The authors are grateful for support from National Key R&D Program of China (No.2023YFB3709900), the National Nature Science Foundation of China (Grant No. U22A20171), the High Steel Center (HSC) at North China University of Technology, University of Science and Technology Beijing.

## CONFLICT OF INTEREST

On behalf of all authors, the corresponding author states that there is no conflict of interest.

## REFERENCES

1. L. Cheng, L. Zhang, Y. Ren, and W. Yang: *Metall. Mater. Trans. B*, 2021, vol. 52, pp. 1186–93.
2. W. Li, Y. Wang, W. Wang, Y. Ren, and L. Zhang: *Metals*, 2020, vol. 10, p. 1205.
3. Y. Wang and C. Liu: *Metall. Mater. Trans. B*, 2022, vol. 53, pp. 2768–73.
4. O. Haida, E. Toshihiko, K. Sanbongi, S. Toshiaki, and A. Fujiwara: *Tetsu-to-Hagane*, 1978, vol. 64, pp. 1538–47.
5. T. Ikeda and H. Ichihashi: *Tetsu-to-Hagane*, 1980, vol. 66, pp. 2040–49.
6. Q. Zhou, J. Ba, W. Chen, and L. Zhang: *Metall. Mater. Trans. B*, 2023, vol. 54, pp. 1565–81.
7. S. Ji, Y. Ren, and L. Zhang: *Steel Res. Int.*, 2023, vol. 94, p. 2200838.
8. Y. Tabatabaei, K. Coley, G. Irons, and S. Sun: *Metall. and Mater. Trans. B.*, 2018, vol. 49, pp. 375–87.
9. N. Verma, P.C. Pistorius, R.J. Fruehan, M. Potter, M. Lind, and S. Story: *Metall. Mater. Trans. B*, 2011, vol. 42, pp. 711–19.
10. L. Zhang, F. Li, and W. Fang: *Steelmaking*, 2016, vol. 32, pp. 1–8.
11. W. Wang, L. Zhang, Y. Ren, Y. Luo, X. Sun, and W. Yang: *Metall. and Mater. Trans. B.*, 2022, vol. 53, pp. 1–7.
12. L. Zhang: *Non-metallic inclusions in steels: fundamentals (in Chinese)*, Metallurgical Industry Press, Beijing, 2019.
13. G. Cheng, L. Zhang, Y. Ren, W. Yang, X. Zhao, and G. Wang: *Steel Res. Int.*, 2021, vol. 92, p. 2000364.
14. M. Li, X. Wang, J. Duan, W. Yang, G. Cheng, L. Wang, L. Yang, and L. Zhang: *Chinese J. Eng.*, 2018, vol. 40, pp. 31–35.
15. X. Wang, X. Li, Q. Li, F. Huang, H. Li, and J. Yang: *Steel Res. Int.*, 2014, vol. 85, pp. 155–63.
16. Z. Deng and M. Zhu: *Iron and steel*, 2023, vol. 58, pp. 104–05.
17. J. Li, M. Jiang, X. He, W. Sun, and X. Wang: *Metall. and Mater. Trans. B.*, 2016, vol. 47, pp. 2386–99.
18. W. Chen, L. Zhang, Y. Wang, Y. Ren, Q. Ren, and W. Yang: *Int. J. Heat Mass Transf.*, 2022, vol. 190, p. 122789.
19. S. Li, X. Xi, X. Zhao, H. Guo, and J. Guo: *J. Iron. Steel Res. Int.*, 2024, vol. 31, pp. 121–33.
20. W. Hu, Q. Zhou, W. Chen, and L. Zhang: *Steel Res. Int.*, 2023, vol. 94, p. 2200709.
21. H. Yin, H. Shibata, T. Emi, and M. Suzuki: *ISIJ Int.*, 1997, vol. 37, pp. 946–55.
22. W. Mu, N. Dogan, and K.S. Coley: *J. Mater. Sci.*, 2018, vol. 53, pp. 13203–15.
23. L. Zheng, A. Malfliet, P. Wollants, B. Blanpain, and M. Guo: *ISIJ Int.*, 2016, vol. 56, pp. 926–35.
24. K. Nakajima and S. Mizoguchi: *Metall. and Mater. Trans. B.*, 2001, vol. 32, pp. 629–41.
25. Y. Deng, L. Zhao, Q. Wang, X. Zhang, and S. He: *Iron and steel*, 2023, vol. 58, pp. 55–66.
26. L. Zeng, Y. Luo, Y. Liu, and C. Zhao: *Iron Steel*, 2023, vol. 58, pp. 67–74.
27. Y. Wang and C. Liu: *Metall. Mater. Trans. B*, 2020, vol. 51, pp. 2585–95.
28. W. Mu, N. Dogan, and K.S. Coley: *Metall. Mater. Trans. B*, 2017, vol. 48, pp. 2092–2103.
29. J. Wang, L. Zhang, Y. Zhang, Q. Ren, and H. Duan: *Metall. Mater. Trans. B*, 2021, vol. 52, pp. 2831–36.
30. H. Duan, Y. Ren, B.G. Thomas, and L. Zhang: *Metall. Mater. Trans. B*, 2019, vol. 50, pp. 36–41.
31. D. Kim, J. Choi, H. Hong, Y. Cho, Y. Park, M. Song, and Y. Kang: *Met. Mater. Int.*, 2022, vol. 28, pp. 3106–19.
32. Z. Qiu, A. Malfliet, B. Blanpain, and M. Guo: *Metall. Mater. Trans. B*, 2022, vol. 53, pp. 1775–91.

33. Z. Qiu, A. Malfliet, B. Blanpain, and M. Guo: *Metall. Mater. Trans. B*, 2022, vol. 53, pp. 1894–1903.
34. R. Gao, L. Wang, C. Chen, S. Yang, X. Li, and Y. Zhang: *J. Iron. Steel Res. Int.*, 2023, vol. 30, pp. 2318–27.
35. R. Li, M. Li, T. Zhang, and W. Wang: *J. Iron. Steel Res. Int.*, 2023, vol. 30, pp. 1952–62.
36. S. Wu, W. Yang, L. Zhang, S. Li, and C. Fu: *China Metall.*, 2022, vol. 32, pp. 36–43.
37. P.A. Kralchevsky, V.N. Paunov, I.B. Ivanov, and K. Nagayama: *J. Colloid Interface Sci.*, 1992, vol. 151, pp. 79–94.
38. L. Wang, S. Yang, J. Li, C. Chen, C. Li, and X. Li: *Steel Res. Int.*, 2021, vol. 92, p. 2100013.

**Publisher's Note** Springer Nature remains neutral with regard to jurisdictional claims in published maps and institutional affiliations.

Springer Nature or its licensor (e.g. a society or other partner) holds exclusive rights to this article under a publishing agreement with the author(s) or other rightsholder(s); author self-archiving of the accepted manuscript version of this article is solely governed by the terms of such publishing agreement and applicable law.